Journal of Energy Chemistry 105 (2025) 87–95

Contents lists available at ScienceDirect

Journal of Energy Chemistry

journal homepage: www.elsevier.com/locate/jechem

http://www.journals.elsevier.com/journal-of-energy-chemistry/

Scalable carbon-patterned layer enhances low-temperature performance of large-format lithium-ion batteries ☆

Jaejin Lim [a,1], Siyoung Park [b,1], Hyobin Lee [b,1], Seungyeop Choi [a], Gwonsik Nam [c], Kyung-Geun Kim [d], Jaecheol Choi [e,*], Young-Gi Lee [e,*], Yong Min Lee [a,b,c,*]

[a] Department of Chemical and Biomolecular Engineering, Yonsei University, 50 Yonsei-ro, Seodaemun-gu, Seoul 03722, Republic of Korea
[b] Department of Energy Science and Engineering, Daegu Gyeongbuk Institute of Science and Technology (DGIST), Daegu 42988, Republic of Korea
[c] Department of Battery Engineering, Yonsei University, 50 Yonsei-ro, Seodaemun-gu, Seoul 03722, Republic of Korea
[d] Energy Science and Engineering Research Center, Daegu Gyeongbuk Institute of Science and Technology (DGIST), Daegu 42988, Republic of Korea
[e] Smart Materials Research Section, Electronics and Telecommunications Research Institute (ETRI)218 Gajeongno, Yuseong-gu, Daejeon 34129, Republic of Korea

ARTICLE INFO

Article history:
Received 30 December 2024
Revised 19 January 2025
Accepted 19 January 2025
Available online 11 February 2025

Keywords:
Low temperature
Electrode design
Carbon-pattern layer
Self-heating
Lithium-ion batteries

ABSTRACT

With electric vehicles (EVs) emerging as a primary mode of transportation, ensuring their reliable operation in harsh environments is crucial. However, lithium-ion batteries (LIBs) suffer from severe polarization at low temperatures, limiting their operation in cold climates. In addition, difficulties in discovering new battery materials have highlighted a growing demand for innovative electrode designs that achieve high performance, even at low temperatures. To address this issue, we prepared a thin, resistive, and patterned carbon interlayer on the anode current collector. This carbon-patterned layer (CPL) serves as a self-heating layer to efficiently elevate the entire cell temperature, thus improving the rate capability and cyclability at low temperatures while maintaining the performance at room temperature. Furthermore, we validated the versatile applicability of CPLs to large-format LIB cells through experimental studies and electrochemo-thermal multiphysics modeling and simulations, with the results confirming 11% capacity enhancement in 21,700 cylindrical cells at a 0.5C-rate and −24℃. We expect this electrode design to offer reliable power delivery in harsh climates, thereby potentially expanding the applications of LIBs.

1. Introduction

Lithium-ion batteries (LIBs) have solidified their position as the primary power source in the electric industry owing to their high energy density, good rate capability, and cyclability [1–3]. However, the operation reliability of LIBs is considered favorable in a moderate temperature range of 15–35℃, with their performance limitedly guaranteed outside this range [4–7]. In particular, under low temperature (LT) conditions, the electrochemical performance of LIBs generally deteriorates significantly owing to their intrinsically sluggish kinetics—correlated with the low ionic conductivity in the electrolyte, high solvation/desolvation energy, large charge transfer resistance at the electrode/electrolyte interface, and slow lithium-ion diffusion in the electrode active materials [8–11]. These sluggish kinetics eventually lead to voltage drops owing to the high polarization inside LIBs, which also promotes lithium plating and dendrite growth by allowing lithium to accumulate preferentially on the electrode surface [12–15]. In particular, considering lithium-ions are generated in metallic form, the total lithium inventory of LIBs is reduced, and metallic lithium may increase the risk of an internal short circuit. Thus, at LTs, LIBs suffer from power and energy loss as well as poor cycle life and safety. Even conventional applications of LIBs, such as portable devices and electric vehicles (EVs), require reliable low-temperature operation [16,17] To further expand their use in military and aerospace applications, reliable operation under harsh environmental conditions must be ensured.

One approach to improve the performance of LIBs at subzero temperatures is to rapidly preheat the cell before cycling. These techniques can be categorized as either external or internal heating. External preheating methods utilize heat sources such as air

---

☆ This article is part of a special issue entitled: 'Innovative battery systems' published in Journal of Energy Chemistry.

* Corresponding authors.

E-mail addresses: jaecheol.choi@etri.re.kr (J. Choi), lyg@etri.re.kr (Y.-G. Lee), yongmin@yonsei.ac.kr (Y.M. Lee).

[1] These authors contributed equally to this work.

https://doi.org/10.1016/j.jechem.2025.01.046

or liquid outside the battery cell [18–20]. Owing to their high feasibility, air and liquid preheating have traditionally been integrated into battery management systems (BMSs) of EVs [21–23]. However, air preheating is considered unsuitable due to the slow heat transfer and additional space requirements for installing equipment, such as fans. Furthermore, liquid preheating requires additional equipment, such as pumps or pipelines, and poses a risk of leakage [24–29]. In contrast, internal heating, which does not require additional parts and leads to rapid and uniform warming within LIB cells, has been intensively investigated. Internal preheating is divided into two categories: self-heating techniques, which use battery energy for self-heating, and current excitation techniques, which generate heat by applying specialized current patterns (e.g., AC and DC pulses). Among them, the self-heating methods are considered highly suitable for large-scale, high-capacity batteries owing to their superior heating efficiency and speed compared to other methods [30–34].

Yang et al. incorporated a Ni foil as a self-heating layer into a 9.5 Ah large-format pouch cell [35,36]. Initially, current was applied only to the Ni foil to rapidly preheat the cell to room temperature (RT), followed by applying a constant current to the cell, enabling it to reach a state of charge (SoC) of 80% within 15 min at −40℃. However, the use of heavy metals and the need for additional wiring may result in barriers, such as reduced energy density and manufacturing complexity. Guan et al. theoretically demonstrated through a numerical model of a 4680 cylindrical cell with a Ni heater foil that heating leads to a more uniform internal temperature distribution than external heating [37]. Furthermore, when internal and external heating were combined, the temperature uniformity improved significantly, confirming the viability of the self-heating layer in large-format cylindrical cells [4,11]. However, fabricating 4680 cylindrical cells is challenging, and the simulation results have not been experimentally validated. Ye et al. introduced a nanoscale heating multilayer on the current collector in an all-solid-state battery system [38], demonstrating a 15-fold increase in power density compared to systems without heating. Through numerical simulations of a 60 kWh battery pack, as the pack size increased, the relative ratio of energy required for heating decreased, thus highlighting the practical applicability of this technology. However, a modulated current collector with a complex five-layer structure cannot be easily utilized in commercial cells.

Thus, in this study, we applied a slurry containing lightweight carbon material to a current collector using a spray coating process. Utilizing a patterned template, a carbon-patterned layer (CPL) was formed, ensuring that the interface between the current collector and composite electrode was not completely blocked. The CPL functioned effectively as a self-heating layer at LTs without acting as a substantial resistive layer at RT. An electrochemical evaluation of pouch cells with CPL was performed to confirm its feasibility in large-format cells, with the results indicating improved rate capability and cyclability at subzero temperatures. Furthermore, electrochemo-thermal multiphysics modeling and simulation theoretically confirmed that the CPL serves as an effective Joule heating source and predicted enhanced rate performance due to rapid self-heating effects in the CPL-included 21,700 cylindrical cell. Hence, this heating architecture promises broad applicability to LIBs and other battery systems.

2. Experimental

2.1. Carbon patterned layer fabrication

To fabricate the carbon-patterned layer (CPL), a slurry was prepared by planetary mixing Super P (Imerys, Switzerland) and sodium carboxymethyl cellulose (Na-CMC; Dai-ichi Kogyo Seiyaku, Japan) at a weight ratio of 90:10 in deionized water. The solid content of the slurry was adjusted to 8% to ensure a uniform coating and prevent nozzle clogging during spray application. A commercial spray coater and an in-house polyetheretherketone (PEEK) patterning mask were used to deposit the CPL onto a 10 μm copper (Cu) current collector (Lotte Energy Materials, Korea). Following spray coating, the CPL was dried at 60 °C for 30 min. The resulting CPL had a mass loading of 0.24 mg cm^{-2} and a thickness of 10 μm.

2.2. Electrode fabrication

The anode slurry was prepared by planetary mixing of artificial graphite (SCMR-AR, Showa Denko, Japan), silicon suboxide (SiO_x, Osaka Titanium Technology, Japan), Super P (Imerys, Switzerland), and a 1:1 mixture of sodium carboxymethyl cellulose (Na-CMC, Dai-ichi Kogyo Seiyaku, Japan) and styrene-butadiene rubber (SBR, BM-400B, Zeon, Japan) at a weight ratio of 91.14:1.86:3:2:2, respectively, using deionized water as the solvent. The slurry was then cast onto Cu foils (10 μm; Lotte Energy Materials, Korea) using a doctor blade, either directly for the bare composite electrode (Bare-e) or onto Cu foils with CPL for the CPL-incorporated composite electrode (CPL-e). The electrodes were dried at 60 °C for 1 h and calendered to achieve a target density of 1.5 g cm^{-3}. The mass loading, excluding the carbon layer, was controlled to 10.9 mg cm^{-2} to ensure a consistent areal capacity of 3.9 mA h cm^{-2} across all anodes.

2.3. Cell assembly

Composite cathodes were prepared by planetary mixing of $LiNi_{0.6}Co_{0.2}Mn_{0.2}O_2$ (NCM622, L&F, Korea), Super P (Imerys, Switzerland), and polyvinylidene fluoride (PVDF, KF1300, Kureha, Japan) in a weight ratio of 96:2:2 in *N*-methyl-2-pyrrolidone (NMP, Sigma-Aldrich, USA). The slurry was cast onto aluminum (Al) foils (15 μm, Sam-A, Republic of Korea) using a doctor blade and dried at 120 °C for 2 h. The cathodes were calendered to a target density of 3.6 g cm^{-3}, with a mass loading and areal capacity of 20.7 mg cm^{-2} and 3.54 mA h cm^{-2}, respectively, resulting in an N/P ratio of approximately 1.1.

The prepared cathodes and anodes were punched into 12 mm and 14 mm diameter disks, respectively, to obtain 2032 coin cells. The electrodes were dried in a vacuum oven at 60 °C for 24 h before assembly. For full cells (SiO_x/graphite||NCM622), an 18 mm polyethylene (PE) separator (F20BHE, 20 μm, Tonen, Japan) and 120 μL of electrolyte—1.15 M $LiPF_6$ in ethylene carbonate (EC) and ethyl methyl carbonate (EMC) (3/7, v/v) with 2 wt% fluoroethylene carbonate (FEC) additive (Enchem, Korea)—were used. For Li||SiO_x/graphite half cells, a 200 μm thick lithium metal foil (Honjo Metal, Japan) punched to a 16.2 mm diameter disk was used as the counter electrode. The assembly process for half the cells was identical to that for the full cells.

Single-layer pouch full cells were assembled in a dry room with a dew point below −60 °C. The prepared SiO_x/graphite anodes and NCM622 cathodes were cut into dimensions of 35 mm × 35 mm and 30 mm × 30 mm, respectively. A PE separator (14 μm, W-Scope Korea, Korea) was punched to dimensions of 40 mm × 40 mm. All components were dried in a vacuum oven at 60 °C for 24 h before assembly. Lead tabs were welded to the electrodes before stacking the anode, separator, and cathode layers within the aluminum (Al) pouch film (150 μm, DNP, Japan). After injecting the same liquid electrolyte used for the coin cells, the cells were sealed under vacuum using a degassing machine.

2.4. Commercial 21,700 cylindrical cell disassembly

The commercial 21,700 cylindrical cells (Si/graphite||$LiNi_{0.8}Co_{0.15}Al_{0.05}O_2$ (NCA) INR 21700-50E, 4.9 Ah discharge capacity, Samsung SDI, Korea) were disassembled in a dry room with a dew point below −60 °C using a saw blade. After disassembly, the electrodes were separated from the jelly roll and washed with dimethyl carbonate (DMC, Enchem, Korea) to remove the residual electrolyte components. The cleaned electrode samples were then vacuum-dried at 25 °C for over 12 h to eliminate any volatile residues before half-cell assembly.

2.5. Electrochemical measurement

Prior to electrochemical evaluation, all cells underwent an aging process: 12 h for coin cells and 24 h for pouch cells, maintained at 25 °C in a constant temperature chamber. Following aging, a two-step pre-cycling procedure was conducted, including one formation cycle and three stabilization cycles to ensure cell stabilization. During the formation cycle, the cell was charged at 0.1 C in constant current (CC) mode up to a 4.3 V cut-off voltage and discharged at the same C-rate to a 3.0 V cut-off voltage. Subsequently, the cell was cycled three times at 0.2 C using a constant current/constant voltage (CC/CV) charge with a 4.3 V cut-off voltage and a 0.02 C cut-off current, followed by discharge at 0.2 C in CC mode to a 3.0 V cut-off voltage. All precycles were performed at 25 °C using a battery cycler (WBCS3000L, Wonatech, Korea).

For Li||Si/graphite and Li||SiO_x/graphite half-cells, the same pre-cycling procedure was applied, except for an operating voltage range of 0.005–1.5 V. For the commercial cylindrical cells, a voltage range of 2.5–4.2 V was used, and testing was performed with a 10-A battery cycler (PEBC05-10, Wonik PNE, Korea). Real-time changes in cell surface temperature were monitored using K-type thermocouples (GL240, Graphtec Corp., Japan). Constant temperature chambers (TC-36S, Yeon Tech, Korea) with an operating temperature range of – 35–100 °C were used for tests conducted at LT (−24 °C).

For the rate capability test of the full cell, the discharge rate was varied from 0.1 to 2 C (0.1, 0.2, 0.5, and 2 C) in the CC mode, whereas the charge rate was fixed at 0.2 C in the CC/CV mode. For the cycle test, a 0.5 C CC/CV charge and discharge modes were employed.

2.6. Electrode characterization

The electronic resistance of the electrodes was measured using an electrode resistance measurement system (RM2610, HIOKI, Japan) within a current range of 0–1 mA and a voltage range of 0–0.5 V. Optical images of the CPL and composite electrodes were captured using confocal microscopy (VHX-900F, Keyence, Japan). The microstructures of the electrodes were analyzed by field-emission scanning electron microscopy (FE-SEM; JSM-7610F-Plus, JEOL, Japan). Electrochemical impedance spectra were acquired using a potentiostat (VMP-300, BioLogic, France) with an amplitude of 10 mV over the frequency range of 5 MHz to 50 mHz. The direct current internal resistance (DCIR) of the half-cell was determined using a hybrid pulse power characterization (HPPC) protocol [39], which involved a 5 C discharge for 10 s, followed by a 40-s rest, 3.75 C discharge for 10 s, another 40-s rest, and a 1.25 C discharge for 10 s. The HPPC measurements were repeated at 10% intervals across states of charge (SoCs) from 20% to 80%. The DCIR value was estimated during the 3.75 C discharge pulse. Galvanostatic intermittent titration technique (GITT) experiments were performed at 0.1 C with 10-min galvanostatic pulses followed by 10-min resting intervals [40,41].

2.7. Electrochemo-thermal multiphysics modeling and simulation

A pseudo-three-dimensional (P3D) electrochemical model coupled with a 3D thermal model for 21,700 cylindrical cells was developed to evaluate electrochemical performance in RT (25 °C) and LT (−24 °C) environments. The electrochemo-thermal multiphysics model was constructed using COMSOL Multiphysics 6.2 (COMSOL. USA) and integrates two simulation physics: a P3D electrochemical model that evaluates the electrochemical behavior of the composite electrode, including CPL, and a 3D thermal model that simulates the thermal behavior of the cell, incorporating the actual internal structure of the 21,700 cylindrical cell (jelly roll). The P3D electrochemical model was based on Doyle and Newman's methodology [42] using a SiO_x/graphite||NCM622 configuration with a separator, current collector, and CPL structures. This model assigns governing equations, including charge conservation, electroneutrality, mass conservation, Fick's law, Ohm's law, and Butler–Volmer equations, for each component. Also, the electrochemical parameters (e.g., exchange current density, diffusion coefficient) were applied to the model as Arrhenius-type functions of temperature. The 3D thermal model employs a microstructure-based modeling method to reflect the jelly roll structure of a cylindrical cell [43]. The temperature changes in the 21,700 cells were simulated by applying heat sources from the P3D electrochemical model to the 3D thermal model. The temperature rise during discharge was cooled by natural heat convection on the cell surface with the standard of 0.5 C discharge condition (h = 10 – 15 W m^{-2} K^{-1}).

3. Results and discussion

3.1. Electrochemical performance of commercial 21,700 cylindrical cells in low- temperature environments

Fig. 1(a)–(d) present the electrochemical performance of a commercial 21,700 cylindrical lithium-ion cell at two operating temperatures: RT (25 °C) and LT (−24 °C). Under RT conditions, although the cell capacity decreased with increasing C-rates, it retained approximately 96.4% of its capacity under a 2 C discharge condition compared to 0.1 C (Fig. 1(a) and (b)). In contrast, at LT, the capacity exhibited a significant decline, maintaining only 87.8% at 0.1 C and further dropping to 54.3% under 2 C discharge conditions (Fig. 1(c) and (d)). The surface temperatures of the cylindrical cells were measured to evaluate the cell temperature changes under various operating conditions (Fig. S1). At RT, the cell surface temperature remained relatively stable at low C rates (0.1, 0.2, and 0.5 C). However, at a higher C-rate of 2 C, the temperature increased to 46.1 °C (an increase of 21.1 °C), enhancing reaction kinetics and enabling discharge capacity similar to that of lower C-rates. In contrast, at LT, even low C rates caused noticeable temperature changes. Specifically, as the C-rate increased from 0.1 to 0.5 C, the cell temperature rose from −21.9 to −12.9 °C, an increase of 9.0 °C. At 2 C, the temperature surged by 32.8 °C compared to that in the 0.1 C condition. This significant temperature increase at LT was attributed to the increased heat generation due to the higher internal resistance. Owing to the abrupt temperature increase, the overpotential was mitigated by improved kinetics, resulting in voltage recovery behavior, particularly under 0.5 and 2 C conditions. These results highlight that the electrochemical performance of the 21,700 cylindrical cells is strongly influenced by the operating and internal temperatures.

Fig. 1(e) shows a schematic representation of the reduced kinetics of the electrochemical reactions under LT conditions. When the cell temperature drops below the ideal range, the lithium-ion conductivity in the electrolyte decreases and the solvation/desolvation

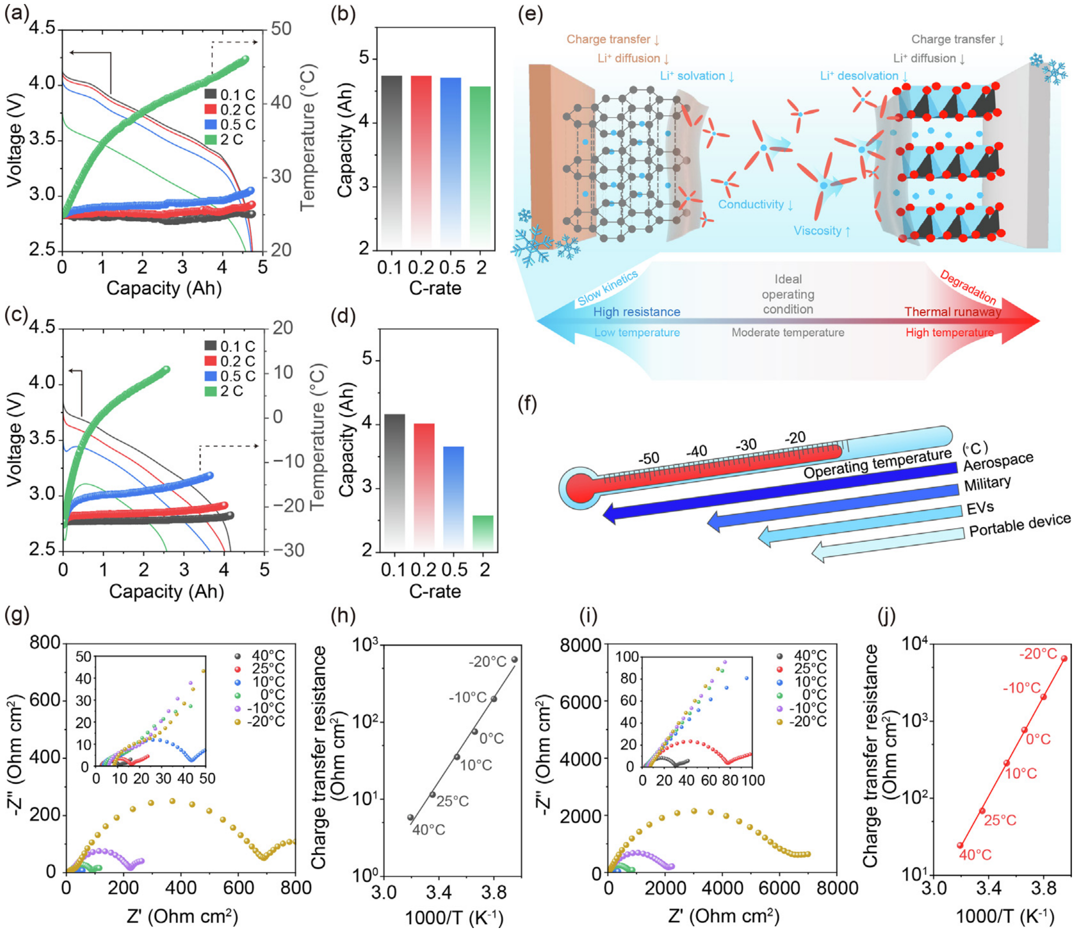

Fig. 1. Voltage and cell temperature profiles of the commercial 21,700 cylindrical cell under varying discharge C-rates at (a) room temperature (RT) (25 °C) and (c) low temperature (LT) (−24 °C). Discharge capacities of commercial 21,700 cylindrical cells at (b) RT and (d) LT. (e) Schematic illustration of the challenges with LIBs below the ideal operating temperature. (f) Potential applications of LIBs and their operating temperature ranges. The EIS spectra of (g) cathode and (i) anode half cells obtained from the commercial 21,700 cylindrical cell as a function of operating temperature. Arrhenius plots of charge transfer resistance derived from EIS spectra for (h) cathode and (j) anode.

processes are substantially hindered. Furthermore, the charge transfer kinetics at the electrode–electrolyte interface slow down, while lithium-ion diffusion within the active material becomes severely restricted [44,45]. Consequently, the performance degradation of LIBs at LTs stems from a comprehensive slowdown of the entire electrochemical process. As shown in Fig. 1(f), the development of advanced materials, electrodes, and cell designs capable of stable operation at LTs is critical for broadening the application range of LIBs, including their use in electric vehicles (EVs) and military and aerospace applications [16,46].

To further investigate the changes in the resistance with temperature, a commercial 21,700 cylindrical cell was disassembled (Fig. S2) to fabricate the Li||NCA and Li||Si/graphite half-cells. Electrochemical impedance spectroscopy (EIS) measurements of these half-cells are shown in Fig. 1(g) and (i). As the temperature decreased from 40 to −20 °C, EIS resistance increased significantly. Using the equivalent circuit model (Fig. S3), the charge-transfer resistance was calculated and plotted as an Arrhenius plot against temperature (Fig. 1(h) and (j)). The results indicate that the resistance changes due to temperature were more pronounced at the anode than at the cathode.

3.2. Self-heating carbon patterned layer for low-temperature operation of LIBs

To enable the stable operation of LIBs at LTs, a carbon pattern layer (CPL) was applied to the anode current collector, where the resistance increases were more pronounced at LTs. As depicted in the schematic in Fig. 2(a), the CPL was fabricated using a perforated pattern mask and spray coater (Fig. S4). The resulting pattern had a diameter of 1 mm and a thickness of 10 μm (Fig. 2(b) and Fig. S5). The CPL, composed of 90 wt% SuperP and 10 wt% CMC binder, demonstrated mechanical robustness, as confirmed by bending and folding tests (Fig. S6). Subsequently, the electrode slurry was cast onto CPL to produce a composite electrode (CPL-e). The electronic conductivities of the three types of composite electrodes were evaluated using a multiprobe electrode resistance measurement system: a bare composite electrode without a carbon layer (Bare-e), a composite electrode with a carbon-patterned layer (CPL-e), and a composite electrode with a uniformly coated carbon layer without patterning (CL-e) (The detailed geometry of each electrode is provided in Fig. S7). As shown in Fig. 2(c), the electronic resistance at the interface between the composite electrode and the current collector more than doubled with the addition of a carbon layer. Notably, the interfacial resistance of CL-e was 29% higher than that of CPL-e, indicating that direct contact between the composite electrode and the current collector minimizes the interfacial resistance. In contrast, a larger coating area of the carbon layer, composed of carbon and a binder, increased the interface resistance. Interestingly, the bulk electronic resistivities of the composite electrodes exhibited a different trend. While CL-e and Bare-e exhibited similar bulk resistivity values (53.0 and 50.6 mOhm cm, respectively), CPL-e displayed a much lower bulk resistivity, reduced by approximately 26.1%. The mass loading

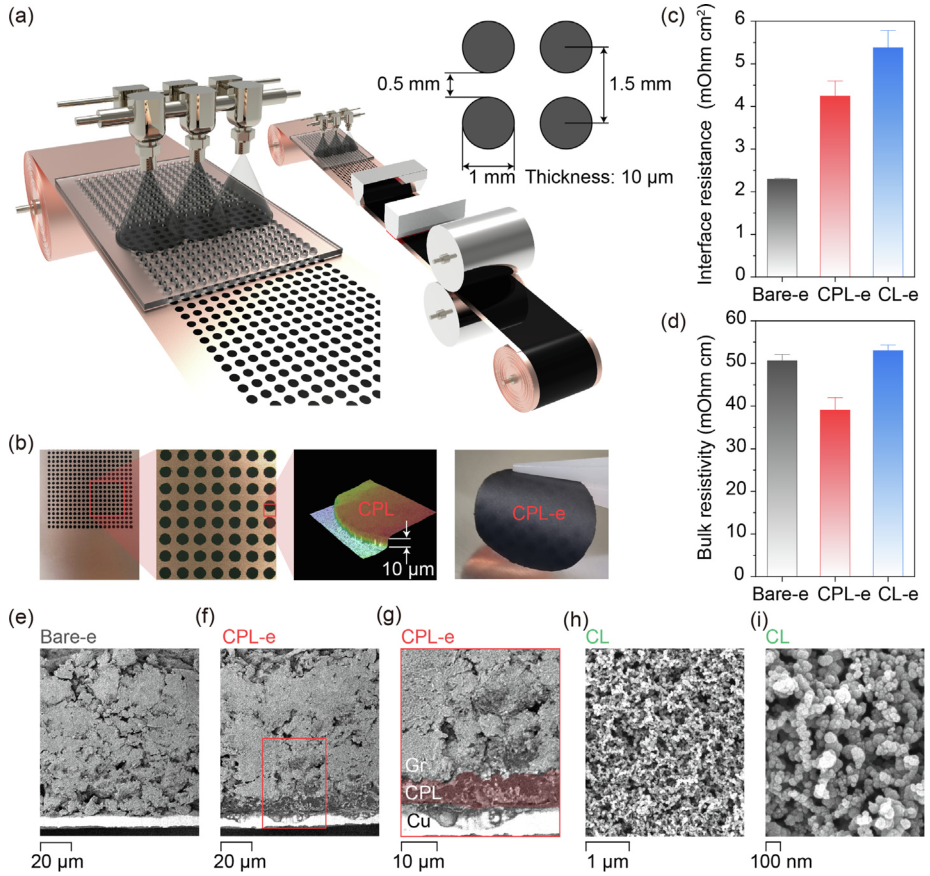

Fig. 2. (a) Schematic illustration of the fabrication process for the carbon-patterned layer (CPL) using a spray coating method, including detailed patterning geometry. (b) Optical images of CPL and CPL-e captured using a digital camera and confocal microscopy. (c) Interfacial electronic resistance between the current collector and composite electrode, and (d) bulk electronic resistivity of the composite electrode for Bare-e, CPL-e, and CL-e. Cross-sectional SEM images (e) of Bare-e and (f, g) CPL-e. (h, i) Top-view SEM images of carbon layer.

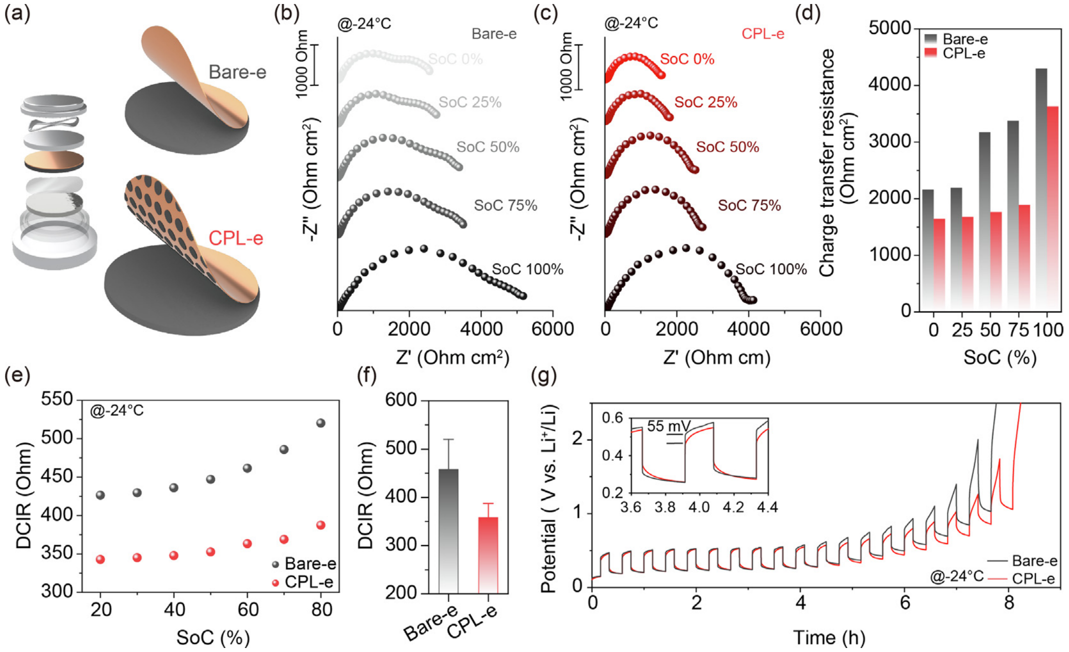

Fig. 3. (a) Schematic illustrations of 2032-type coin cell assembled with Bare-e or CPL-e. EIS spectra of (b) Bare-e and (c) CPL-e at different states of charge (SoCs). (d) Charge transfer resistance derived from the EIS spectra of Bare-e and CPL-e. (e) Direct current internal resistance (DCIR) of Bare-e and CPL-e as a function of SoC, estimated using the hybrid pulse power characterization (HPPC) technique. (f) Average DCIR of Bare-e and CPL-e across different SoCs. (g) Galvanostatic intermittent titration technique (GITT) curves for Bare-e and CPL-e.

and density of all composite electrodes, excluding the carbon layer, were controlled to identical values of 10.9 mg·cm^{-2} and 1.5 g·cm^{-3}. Hence, the Bare-e and CL-e can be considered to exhibit comparable bulk resistivities. However, the reduced bulk resistivity of CPL-e is probably due to localized density variations within the composite electrode, resulting from the presence of the 10-µm-thick CPL. The relatively high-density region on top of the CPL may decrease overall bulk electronic resistivity. Fig. 2(e)–(g) provide cross-sectional SEM images of Bare-e and CPL-e, clearly showing the SiO_x/graphite composite electrode and the approximately 10-µm-thick CPL. Notably, the composite electrode coated over the CPL exhibits lower porosity compared to Bare-e. Additionally, as shown in Fig. 2(h) and (i), the internal carbon network of the CL was distinctly visible.

To evaluate the impact of the CPL on electrochemical performance, we fabricated Li||Bare-e and Li||CPL-e 2032-type coin cells (Fig. 3(a)) and measured their electrode resistance at LT (−24 °C). Electrochemical impedance spectroscopy (EIS) was conducted across various states of charge (SoCs) by increasing the SoC from 0% to 100% in 25% intervals. The results show that the EIS resistance of CPL-e (Fig. 3(c)) is consistently lower than that of Bare-e (Fig. 3(b)) at all SoC levels. Moreover, charge-transfer resistance (R_{ct}) analysis using an equivalent circuit model (Fig. S2) revealed a 44.5% reduction in the R_{ct} at 50% SoC in the presence of CPL (Fig. 3(d)). Similar trends were observed for hybrid pulse power characterization (HPPC) and galvanostatic intermittent titration technique (GITT) (Fig. S8). As shown in Fig. 3(e), the direct current internal resistance (DCIR) obtained through HPPC was, on average, 22% lower for CPL-e than for Bare-e across the SoC range of 20%–80% (358 Ohm vs. 458 Ohm, respectively; Fig. 3(f)). Additionally, GITT measurements revealed consistently lower overpotentials for CPL-e than for Bare-e. In particular, within the low-voltage plateau region, Bare-e displays an overpotential of approximately 55 mV higher than that of CPL-e, causing it to reach the cut-off voltage more quickly. Given that Bare-e and CPL-e exhibited similar capacities and comparable DCIR values at RT (Figs. S9 and S10), CPL appears to have a more pronounced effect on electrochemical performance, such as rate capability and capacity reten-

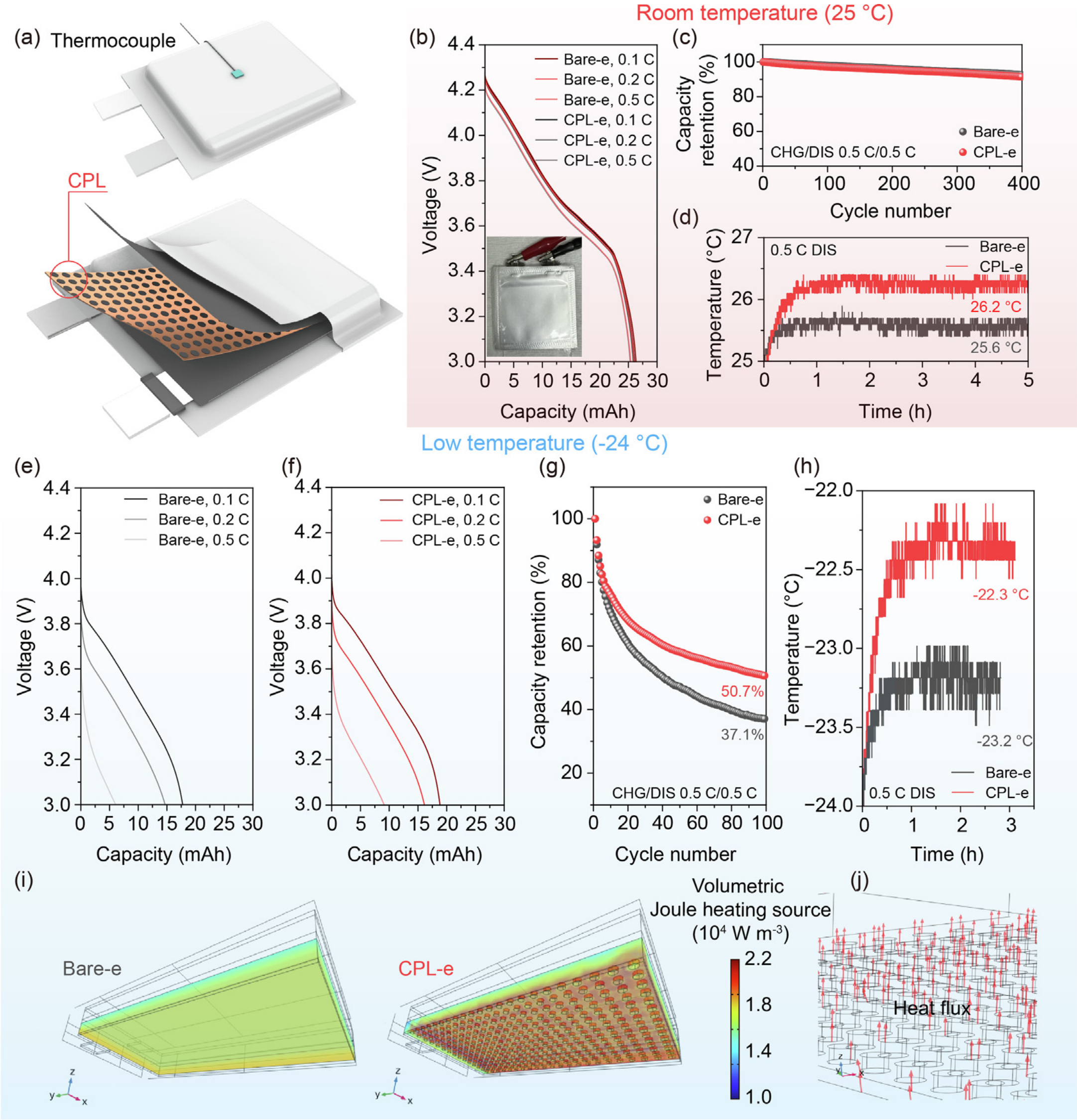

Fig. 4. (a) Schematic illustrations of pouch cell assembled with CPL-e and experiment setup to measure cell temperature. (b) Voltage profiles of Bare-e and CPL-e at varying discharge C-rates at RT (25 °C). (c) Capacity retention curves of Bare-e and CPL-e at RT. (d) Cell temperature profiles under 0.5C discharge condition at RT. Voltage profiles of (e) Bare-e and (f) CPL-e at varying discharge C-rates. (g) Capacity retention curves, and (h) cell temperature profiles at LT (−24 °C). (i) Volumetric Joule heating source of Bare-e and CPL-e and (j) heat flux of CPL-e.

tion, at LT than at RT. To further investigate this observation, we fabricated Bare-e ||NCM622 and CPL-e||NCM622 full cells to evaluate their performance under both conditions.

Fig. 4(a) shows a schematic of a pouch cell equipped with a CPL and thermocouple to monitor the temperature changes during discharge. At RT, Bare-e and CPL-e exhibited comparable capacity and voltage profiles (Fig. 4(b)). Even after 400 charge/discharge cycles (0.5 C constant current discharge and 0.5 C constant current/constant voltage charge), both cells exhibited similar capacity retention of 91.9% and 90.7% for Bare-e and CPL-e, respectively (Fig. 4(c)), indicating that CPL does not function as a severe resistive layer that negatively affects electrochemical performance at RT. Consistently, thermocouple measurements at the end of a 0.5 C discharge showed minimal temperature differences, with Bare-e reaching 25.6 °C and CPL-e 26.2 °C, a modest rise of only 0.6 °C (Fig. 4(d)). In contrast, significant differences emerged under LT conditions (−24 °C). Fig. 4(e) and (f) show the voltage profiles of Bare-e and CPL-e at various C-rates. The CPL enhanced discharge capacity, with increases of 6.2%, 10.1%, and 50.0% at 0.1, 0.2, and 0.5 C, respectively, alongside a reduction in initial overpotential. This improved performance was also evident in the LT cyclability tests (Fig. 4(g)). After 100 cycles (0.5 C constant current discharge and 0.5 C constant current/constant voltage charge), Bare-e retained only 37.1% of its initial capacity, whereas CPL-e achieved a higher retention of 50.7%, indicating an approximate 40% improvement. The post-cycling analysis of the anode surface (Fig. S11) revealed pronounced Li plating on Bare-e, whereas CPL-e exhibited reduced Li deposition. These findings suggest that CPL improves the rate capability by reducing the overpotential and mitigates lithium plating, thereby enhancing cycle retention.

Surface temperature analysis of the pouch cells (Fig. 4(h)) further highlights the impact of CPL. During operation, CPL-e exhibited a temperature rise approximately 1.1 °C higher than Bare-e, double the temperature difference observed at RT. Discharge simulations that accounted for the actual electronic resistivity (Fig. S12) and CPL geometry (Fig. S13) confirmed that the CPL acted as a self-heating layer (Fig. 4(i)) and the heat flux from the CPL to the electrode (Fig. 4(j)). In summary, while the CPL had a negligible impact on the RT performance compared to Bare-e, it significantly improved the rate capability and cyclability under LT conditions, as the CPL effectively increased the cell temperature as a self-heating layer.

3.3. Electrochemo-thermal behavior of large-format lithium-ion cell with carbon-pattern layer

As shown in Fig. 4(h), the thermocouple only measured the surface temperature of the pouch cell. Given the observed enhancements in electrochemical performance following the introduction of CPL, the actual internal temperature of the operating cell is likely to be even higher. This temperature elevation is expected to be more pronounced in high-capacity large-format cells. However, the direct measurement of the internal cell temperature during operation poses significant difficulties. Furthermore, manufacturing high-capacity cells in small quantities poses significant challenges in ensuring reliability. To address these limitations, we conducted electrochemo-thermal multiphysics simulations to estimate the internal temperature changes and electrochemical performance in a 21,700 cylindrical cell with a CPL (Fig. 5(a)). Details of the 3D electrochemo-thermal model, including cell geometry (Fig. S14), symbols (Table S1), governing equations (Table S2), and parameters (Tables S3 and S4) are provided in Supplementary Information.

Fig. 5(b) and (c) present the voltage and average internal cell temperature profiles of the Bare-e 21,700 and CPL-e 21,700 cells at RT at various C-rates. Both cell types demonstrated comparable capacities, consistent with the experimental results observed in the pouch cells. However, the internal temperature of CPL-e 21,700 was slightly higher than that of Bare-e 21700; this difference became more distinctive at higher C-rates. Under 2 C discharge conditions, CPL-e 21,700 exhibited an internal temperature approximately 2.1 °C higher than Bare-e 21,700 (48.4 °C vs. 46.3 °C). This increase contributed to the reduced overpotential and slight improvement in capacity during the later

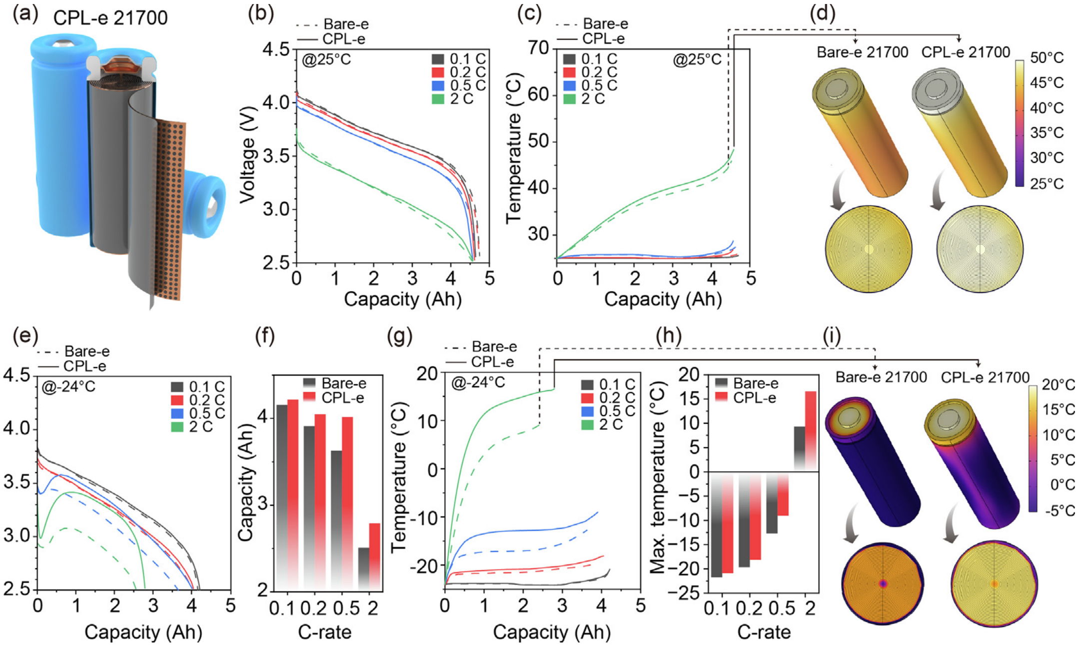

Fig. 5. (a) Schematic illustrations of 21,700 cylindrical cells assembled with CPL-e. (b) Simulated voltage and (c) cell temperature profiles at varying discharge C-rates of Bare-e and CPL-e at RT (25 °C). (d) Simulated cell temperature 3D color maps for Bare-e 21,700 and CPL-e 21,700 at the end of 2C discharge process at RT. (e) Simulated voltage profiles, (f) discharge capacities, (g) temperature profiles, and (h) maximum average cell temperatures at varying discharge C-rates under LT (−24 °C) conditions of Bare-e 21,700 and CPL-e 21700. (i) Simulated cell temperature 3D color maps for Bare-e 21,700 and CPL-e 21,700 at the end of 2C discharge process at LT.

stages of the 2 C discharge. Despite these differences, as shown in Fig. 5(d), the temperature distribution within the jelly roll at the end of the 2 C discharge process was similar for both cells, indicating a minimal internal temperature gradient. Under LT (−24 °C) conditions, the voltage and average internal cell temperature profiles of Bare-e 21,700 and CPL-e 21,700 displayed significant differences. As shown in Fig. 5(e), CPL-e 21,700 exhibited a lower initial overpotential than Bare-e 21700. Particularly at 0.5 C and 2 C discharge rates, CPL-e 21,700 demonstrated a more substantial recovery in voltage drop due to the temperature increase, highlighting the effectiveness of CPL in mitigating the overpotential. Consequently, the average discharge capacity of CPL-e 21,700 was, on average, 6.7% higher than that of Bare-e 21700. Notably, at 0.5 C, the improvement reached 11.2%, underscoring the potential for substantial capacity gains in large-format cells with CPL (Fig. 5(f)). As indicated by the voltage recovery trends, the average internal temperature of the 21,700 cylindrical cells increased significantly at higher discharge rates (Fig. 5(g)). For CPL-e 21700, the internal temperature rose sharply from −24 °C to approximately 10 °C during the initial stages of 2 C discharge, demonstrating the CPL's role as an effective self-heating layer. This rapid increase in temperature (14.0 °C min^{-1} for CPL-e 21,700 compared to 5.9 °C min^{-1} for Bare-e 21700) contributes to the improved capacity. By the end of discharge, the internal temperature of CPL-e 21,700 exceeded that of Bare-e 21,700 by 0.8, 1.5, 3.7, and 7.6 °C at 0.1, 0.2, 0.5, and 2 C rates, respectively (Fig. 5(h)). Additionally, as shown in Fig. 5(i), CPL-e 21,700 exhibited a more uniform temperature distribution at a 2 C discharge rate, further highlighting its thermal management benefits compared to other self-heating strategies (Table S5).

4. Conclusions

With commercial 21,700 cylindrical cells, we identified that LT environments hinder electrochemical reactions, resulting in high overpotentials and poor performance. We developed a carbon-patterned layer (CPL) as a self-heating solution to enhance the operational reliability of LIBs under extreme temperature conditions. Fabricated via a spray-coating process, the CPL demonstrated effectiveness in rapidly and efficiently elevating cell temperatures. The experimental results across various cell formats confirmed significant improvements in the electrochemical performance at LTs. Specifically, at −24 °C, the pouch cell with CPL achieved a 50% increase in 0.5 C discharge capacity and a 40% enhancement in 0.5 C cycle retention. Additionally, 3D electrochemo-thermal multiphysics modeling and simulations demonstrated the effectiveness of CPL in large-format cells. When incorporated into 21,700 cylindrical cell models, the CPL delivered up to an 11% increase in capacity under −24 °C and 0.5 C discharge conditions, with no observable performance degradation at RT. These findings highlight the potential of CPLs as practical solutions for improving the LT performance of LIBs. This study provides a foundational framework for integrating internal self-heating layers to enhance the LIB operability in challenging thermal environments.

CRediT authorship contribution statement

Jaejin Lim: Writing – original draft, Visualization, Software, Methodology, Investigation, Formal analysis, Data curation, Conceptualization. **Siyoung Park:** Software, Methodology, Investigation, Formal analysis. **Hyobin Lee:** Writing – original draft, Methodology, Investigation. **Seungyeop Choi:** Methodology, Investigation, Formal analysis. **Gwonsik Nam:** Methodology, Investigation. **Kyung-Geun Kim:** Methodology, Investigation. **Jaecheol Choi:** Writing – review & editing, Supervision, Project administration, Data curation. **Young-Gi Lee:** Writing – review & editing, Supervision, Resources, Funding acquisition. **Yong Min Lee:** Writing – review & editing, Writing – original draft, Supervision, Resources, Project administration, Investigation, Funding acquisition, Conceptualization.

Declaration of competing interest

The authors declare that they have no known competing financial interests or personal relationships that could have appeared to influence the work reported in this paper.

Acknowledgments

This research was financially supported by the Institute of Civil Military Technology Cooperation funded by the Defense Acquisition Program Administration and Ministry of Trade, Industry and Energy of Korean government under grant No. 22-CM-FC-20. The authors are grateful for the support from the DGIST Supercomputing and Bigdata Center.

Appendix A. Supplementary material

Supplementary data to this article can be found online at https://doi.org/10.1016/j.jechem.2025.01.046.

References

[1] F. Degen, M. Winter, D. Bendig, J. Tübke, Nat. Energy 8 (2023) 1284–1295.
[2] F. Duffner, N. Kronemeyer, J. Tübke, J. Leker, M. Winter, R. Schmuch, Nat. Energy 6 (2021) 123–134.
[3] X.G. Yang, T. Liu, C.Y. Wang, Nat. Energy 6 (2021) 176–185.
[4] S.H. Park, J. Park, M.H. Ryou, Y.M. Lee, J. Power Sources 465 (2020) 228238.
[5] W. Wu, S. Wang, W. Wu, K. Chen, S. Hong, Y. Lai, Energy Convers. Manag. 182 (2019) 262–281.
[6] N. Piao, X. Gao, H. Yang, Z. Guo, G. Hu, H.M. Cheng, F. Li, Etransportation 11 (2022) 100145.
[7] J. Jaguemont, L. Boulon, Y. Dubé, Appl. Energy 164 (2016) 99–114.
[8] Y. Qin, P. Zuo, X. Chen, W. Yuan, R. Huang, X. Yang, J. Du, L. Lu, X. Han, M. Ouyang, J. Energy Chem. 72 (2022) 442–452.
[9] T. Waldmann, M. Wilka, M. Kasper, M. Fleischhammer, M. Wohlfahrt-Mehrens, J. Power Sources 262 (2014) 129–135.
[10] P. Bai, J. Li, F.R. Brushett, M.Z. Bazant, Energy Environ. Sci. 9 (2016) 3221–3229.
[11] D. Hu, G. Chen, J. Tian, N. Li, L. Chen, Y. Su, T. Song, Y. Lu, D. Cao, S. Chen, F. Wu, J. Energy Chem. 60 (2021) 104–110.
[12] M. Petzl, M. Kasper, M.A. Danzer, J. Power Sources 275 (2015) 799–807.
[13] G. Zhang, X. Wei, G. Han, H. Dai, J. Zhu, X. Wang, X. Tang, J. Ye, J. Power Sources 484 (2021) 229312.
[14] X. Lin, K. Khosravinia, X. Hu, J. Li, W. Lu, Prog. Energy Combust. Sci. 87 (2021) 100953.
[15] Q. Liu, C. Du, B. Shen, P. Zuo, X. Cheng, Y. Ma, G. Yin, Y. Gao, RSC Adv. 6 (2016) 88683–88700.
[16] N. Zhang, T. Deng, S. Zhang, C. Wang, L. Chen, C. Wang, X. Fan, Adv. Mat. 34 (2022) 2107899.
[17] P. Lu, Z. Zhou, Z. Xiao, J. Lu, J. Zhang, G. Hu, W. Yan, S. Xia, S. Zhang, Z. Wang, H. Li, C. Wang, F. Wu, X. Sun, Joule 8 (2024) 635–657.
[18] C. Tang, P. Yuan, Z. Cen, Z. Yin, Y. Yan, Z. Xie, J. Phys. Conf. Ser. 2823 (2024) 012036.
[19] F. Larsson, B.-E. Mellander, J. Electrochem. Soc. 161 (2014) A1611–A1617.
[20] P.V. Chombo, Y. Laoonual, J. Loss Prev. Process Ind. 79 (2022) 104855.
[21] H. Rahimi-Eichi, U. Ojha, F. Baronti, M.Y. Chow, IEEE Ind. Electron. Mag. 7 (2013) 4–16.
[22] C. Zhu, L. Du, B. Guo, G. Fan, F. Lu, H. Zhang, IEEE T. Transp. Electr. 9 (2023) 5012–5027.
[23] S. Mishra, S.C. Swain, R.K. Samantaray, In: 2021 International Conference on Advances in Computing and Communications (ICACC), Kochi, Kakkanad, India, (2021) 1–6.
[24] X. Hu, Y. Zheng, D.A. Howey, H. Perez, A. Foley, M. Pecht, Prog. Energy Combust. Sci. 77 (2020) 100806.
[25] Y. Wang, X. Zhang, Z. Chen, Appl. Energy 313 (2022) 118832.
[26] Y. Wang, Z. Rao, S. Liu, X. Li, H. Li, R. Xiong, Appl. Therm. Eng. 190 (2021) 116811.
[27] J. Bao, Z. Zhou, W.T. Wu, L. Wei, J. Lyu, Y. Li, H. Huang, Y. Li, Y. Song, Case Stud. Therm. Eng. 60 (2024) 104759.
[28] C. Zhang, J. Huang, W. Sun, X. Xu, C. Li, Y. Li, J. Energy Storage 55 (2022) 105497.

[29] Z. Ye, X. Fu, S. Zhou, Appl. Therm. Eng. 245 (2024) 122770.
[30] J. Li, S. He, Q. Yang, Z. Wei, Y. Li, H. He, IEEE T. Transp. Electr. 9 (2023) 4824–4845.
[31] S.H. Ha, J.I. Lee, H. Yoon, T.R. Park, J. Baek, J.S. Kim, G.W. Moon, IEEE Trans. Aerosp. Electron. Syst. 58 (2022) 3399–3410.
[32] H. Ruan, J.V. Barreras, M. Steinhardt, A. Jossen, G.J. Offer, B. Wu, J. Power Sources 581 (2023) 233484.
[33] J. Xu, X. Mei, H. Wang, J. Wang, IEEE Trans. Industr. Inform. 17 (2021) 4714–4723.
[34] H. Ruan, B. Sun, T. Zhu, X. He, X. Su, A. Cruden, W. Gao, Appl. Therm. Eng. 186 (2021) 116158.
[35] X.G. Yang, T. Liu, C.Y. Wang, J. Power Sources 342 (2017) 598–604.
[36] X.G. Yang, G. Zhang, S. Ge, C.Y. Wang, Proc. Natl. Acad. Sci. U S A 115 (2018) 7266–7271.
[37] C. Guan, H. Szeto, O. Wander, V. Kumar, R.J. Clément, Y. Zhu, Nano Res. 17 (2024) 8794–8802.
[38] Y. Ye, W. Huang, R. Xu, X. Xiao, W. Zhang, H. Chen, J. Wan, F. Liu, H.K. Lee, J. Xu, Z. Zhang, Y. Peng, H. Wang, X. Gao, Y. Wu, G. Zhou, Y. Cui, Adv. Mater. 34 (36) (2022) 2202848.
[39] S. Choi, N. Kim, D. Jin, Y. Roh, D. Kang, H. Lee, S.T. Hong, H. Lee, Y.M. Lee, J. Power Sources 579 (2023) 233265.
[40] J. Kim, S. Park, S. Hwang, W.S. Yoon, J. Electrochem. Sci. Technol. 13 (2022) 19–31.
[41] W. Weppner, R.A. Huggins, J. Electrochem. Soc. 124 (1977) 1569.
[42] M. Doyle, J. Newman, A.S. Gozdz, C.N. Schmutz, J.-M. Tarascon, J. Electrochem. Soc. 143 (1996) 1890–1903.
[43] S. Park, H. Lee, S. Choi, J. Lim, S. Kim, J. Song, M. Ali, T.S. Kwon, C. Doh, Y.M. Lee, Etransportation 22 (2024) 100370.
[44] A. Hu, F. Li, W. Chen, T. Lei, Y. Li, Y. Fan, M. He, F. Wang, M. Zhou, Y. Hu, Y. Yan, B. Chen, J. Zhu, J. Long, X. Wang, J. Xiong, Adv. Energy. Mater. 12 (2022) 2202432.
[45] M. Qin, Z. Zeng, S. Cheng, J. Xie, Interdiscip. Mater. 2 (2023) 308–336.
[46] Z. Hong, H. Tian, Z. Fang, Y. Luo, H. Wu, F. Zhao, Q. Li, S. Fan, J. Wang, ChemElectroChem 11 (2024) e202300759.